Original Article

Preservation of the naïve features of mesenchymal stromal cells in vitro: Comparison of cell- and bone-derived decellularized extracellular matrix

Journal of Tissue Engineering
Volume 13: 1–20

DOI: 10.1177/20417314221074453
journals.sagepub.com/home/tej
SAGE

Ana Rita Pereira[1,2], Drenka Trivanović[1,2], Philipp Stahlhut[3], Maximilian Rudert[4], Jürgen Groll[3] and Marietta Herrmann[1,2]

Abstract

The fate and behavior of bone marrow mesenchymal stem/stromal cells (BM-MSC) is bidirectionally influenced by their microenvironment, the stem cell niche, where a magnitude of biochemical and physical cues communicate in an extremely orchestrated way. It is known that simplified 2D in vitro systems for BM-MSC culture do not represent their naïve physiological environment. Here, we developed four different 2D cell-based decellularized matrices (dECM) and a 3D decellularized human trabecular-bone scaffold (dBone) to evaluate BM-MSC behavior. The obtained cell-derived matrices provided a reliable tool for cell shape-based analyses of typical features associated with osteogenic differentiation at high-throughput level. On the other hand, exploratory proteomics analysis identified native bone-specific proteins selectively expressed in dBone but not in dECM models. Together with its architectural complexity, the physico-chemical properties of dBone triggered the upregulation of stemness associated genes and niche-related protein expression, proving in vitro conservation of the naïve features of BM-MSC.

Keywords

Decellularization, bone model, stem cell niche, stemness, osteogenesis, 3D models

Date received: 12 November 2021; accepted: 4 January 2022

Introduction

Mesenchymal stem/stromal cells (MSC) are rare, self-renewing, multipotent cells, responsible for maintaining skeletal tissues' homeostasis. Since the discovery of MSC in bone marrow (BM),[1] similar cell populations with proliferative competence, an undifferentiated phenotype and the ability to differentiate into osteoblastic, adipogenic, and chondrogenic lineages in vitro, have been identified and reported in many adult[2–4] and perinatal tissues.[5–7] Due to MSC's ability to colonize and differentiate into a multitude of tissue and cell types, these cells are suitable candidates to treat many degenerative congenital abnormalities and diseases.[8] Although widely distributed, it seems that MSC are not uniform populations. Moreover, literature exists demonstrating that stem cell fate of MSC is highly dependent and controlled by the tissue-specific surrounding environment,[9] and perturbations in the matrix as a result of inflammation or disease progression.[10,11] In fact, adult tissues retain unique milieus, known as stem cell niches, defined by their anatomic location and protective surrounding, where multipotent cells are self-maintained in quiescence and/or mobilized in response to stimuli. The niche is a dynamic structure that transmits and receives

[1]IZKF Group Tissue Regeneration in Musculoskeletal Diseases, University Hospital Wuerzburg, Wuerzburg, Germany
[2]Bernhard-Heine-Centrum for Locomotion Research, University of Wuerzburg, Wuerzburg, Germany
[3]Chair for Functional Materials in Medicine and Dentistry and Bavarian Polymer Institute, University of Wuerzburg, Wuerzburg, Germany
[4]Department of Orthopedic Surgery, Koenig-Ludwig-Haus, University of Wuerzburg, Wuerzburg, Germany

Corresponding author:
Marietta Herrmann, IZKF Group Tissue Regeneration in Musculoskeletal Diseases, University Hospital Wuerzburg and Bernhard-Heine-Centrum for Locomotion Research, University of Wuerzburg, Röntgenring 11, Wuerzburg, Bayern 97070, Germany.
Email: m-herrmann.klh@uni-wuerzburg.de

signals through cellular and acellular mediators, where the interplay between MSC and neighboring cells of different maturation and activation states likewise plays a pivotal role in tissue dynamics.[12] These niches protect stem cells from depletion during adult life, preventing their uncontrolled proliferation and differentiation. The concept of a stem cell niche has become more complex since its first definition was proposed by Schofield in 1978 in the context of the hematopoietic microenvironment[13]; stem cell niches constitute a basic unit of tissue physiology, with not only well-defined anatomical but also with functional dimensions. A primary function of the niche is to provide physical anchorage to stem cells, mainly via RGD-mediated adhesion molecules.[14] In BM, the location and identification of MSC is controversially discussed due to the lack of distinct surface markers to identify these cells in vivo. Recent studies suggested that at least three different osteoblastic niches for skeletal progenitor cells exist, in particular at endosteal, perivascular, and stromal regions (reviewed in Herrmann and Jakob[11]), implying distinct functions in tissue maintenance and regeneration.[15] It is clear that standard in vitro monolayer culture approaches do not recapitulate this environmental complexity, thus causing a widely observed translational gap from in vitro results to the in vivo situation and clinics. Moreover, from a biochemical perspective, the niche-specific extracellular matrix (ECM) regulates stem cell fate in an extremely well-orchestrated manner,[16] triggering intracellular signaling pathways either by (1) directly binding to cellular receptors, or indirectly (2) presenting non-canonical growth factors, and (3) generating stress gradients of, for example, oxygen content or mechanical forces due to its physical properties and spatial orientation. In fact, the ECM network is not an arbitrary arrangement of structural proteins. Common ECM proteins such as collagens, fibronectin, vitronectin, and proteoglycans exhibit conserved motifs assigned to keenly bind several growth factors and bone morphogenic proteins (BMPs), hence acting as an insoluble localized reservoir of morphogens.[17,18] Meanwhile, proteolytic enzymes, such as matrix metalloproteinases (MMPs), locally break ECM proteins, resulting in a confined release of soluble growth factors from their insoluble anchorage.[19,20] Likewise, physical properties of the microenvironment such as stiffness, porosity and topography are also constantly being remodeled and may as well influence various anchorage-related biological functions, such as cell division, tissue polarization, and cell migration.[21,22] Importantly, all these characteristics and properties are intrinsically related and can mutually influence each other. This becomes even more evident when one considers cell-ECM communication (or relations) as bidirectional interactions, wherein cells constantly rebuild their surroundings, thus untimely influencing their own fate.[23–25] It follows from this that great efforts have been made in the field of tissue engineering using advanced biomaterials to recapitulate these unique niche conditions in *ex vivo* culture. The key universal goal is to avoid the persistently observed "ageing" process of cells during long-lasting in vitro cultivation – that is, cell shape change, and significantly decreased colony-forming and differentiation potential.[26,27] Indeed, it is now widely recognized that 2D cultures, despite their numerous advantages in regard to simplicity, impose artificial spatial limits to cell-matrix interactions and mechanical transduction processes. Consequently, those limitations ultimately strongly influence cell biological functions and response to stimuli,[28] resulting in potentially misleading results toward clinic applications. A wide variety of material alternatives have been developed to recreate the tissue-specific ECM composition and intricate structure of stem cell niches,[29–32] albeit a single in vitro model that reproduces the in vivo microenvironment homeostasis remains a bioengineering challenge. Aiming to address this issue, decellularization of cell-derived ECM, tissues, and organs came as an ideal reverse-engineering concept able to faithfully mimic the native tissue complexity. Through physical, chemical and/or enzymatic treatments, the central goal of decellularization protocols is to preserve the above-mentioned biochemical complexity and mechanical integrity of the tissue, while efficiently removing all cellular elements to prevent any immunological reaction.[33] Decellularized tissue constructs have been successfully applied for several years in tissue engineering and regenerative medicine, mainly designed for rather simple tissues, for example, heart valve substitutes,[34,35] skin grafts,[36,37] bladder mucosa grafts,[38,39] etc. Particularly, decellularized bone ECM-derived constructs – for example, (1) in vitro MSC-produced decellularized ECM constructs[40] and (2) bioactive 3D scaffolds originated from trabecular[41,42] or cortical decellularized bone[43] — have gained a lot of interest as implantable biomaterials for bone tissue repair and regeneration, due to their biochemical properties and their unique mechanical properties and architecture.

To date, the simplest models for examining biological behavior of MSC in response to microenvironmental factors are conducted in 2D monocultures.[44] Although very convenient and effective for mechanistic purposes, the results from 2D culture models may not represent the essential and complex physical features of native microenvironments. Therefore, in this study, we developed and systematically compare unique human bone ECM models (2D and 3D) based on decellularization techniques, aiming to identify intrinsic ECM regulatory factors in either basal or osteogenic settings, which may be responsible for maintenance of MSC stem-cell competence in vitro and their response to homeostatic and extrinsic signals. Thus, the novelty of this study lays on the systematic approach aiming to verify the physiological relevance of 2D in vitro produced decellularized models, commonly used in

literature, by a direct comparison with a human tissue-derived decellularized matrix.

Materials and methods

BM-MSC isolation and expansion

MSC were isolated from human BM acetabular reaming of patients undergoing hip arthroplasty surgery after obtaining informed consent of the patient (Ethical approval (187/18)). Briefly, mononuclear cells were collected from BM material by Ficoll (Histopaque®-1077, Sigma-Aldrich, Germany) density gradient centrifugation (150 RCF for 5 min, Heraeus Multifuge X1R Centrifuge, Thermo Fisher Scientific, Germany) and repeatedly washed. To obtain adherent BM-MSC fraction, cells were cultured and further expanded in culture medium (DMEM/F-12 GlutaMAX, 31331-028, Gibco, Germany) supplemented with 10% fetal calf serum (FCS, Bio&Sell, Germany), 1% Pen/Strep (P4333, Gibco), 1% HEPES (H0887, Sigma-Aldrich), and 5 ng/mL fibroblast growth factor (FGF, 100-18C, PeproTech, Germany) at 37°C in a humidified atmosphere and 5% CO_2. Culture medium was replaced three times a week. Cells were detached from culture flasks by trypsinization (T4174, Sigma-Aldrich), centrifuged and washed. Cell number and viability were assessed with the trypan-blue dye (93595, Sigma-Aldrich) exclusion test. BM-MSC in passage 4–6 were used for the experiments.

2D decellularized matrices (dECM) production

We often observed delamination of newly formed ECM of decellularization cultures on conventional tissue culture plastic well plates (data not shown). In order to achieve robustly anchored native dECM, BM-MSC were seeded on 13 mm treated-coverslips (174950, Thermo Scientific Nunc, USA) at a density of 2×10^4 cells/cm^2. Cells were cultivated for an accommodation period of 48 h in DMEM/F-12 GlutaMAX medium supplemented with 10% FCS, 1% Pen/Strep and 1% HEPES, before starting the matrix production phase. Four different models were created combining two variables: the time of culture (10 or 21 days) and media supplementation (basal: DMEM/F-12 GlutaMAX medium supplemented with 10% FCS, 1% Pen/Strep, 1% HEPES, and 50 µg/mL L-Ascorbic acid 2-phosphate (ASC, A8960, Sigma-Aldrich); osteo: DMEM low glucose medium (D6046, Sigma-Aldrich) supplemented with 10% FCS, 1% Pen/Strep, 1% HEPES, 50 µg/mL ASC, 5 mM β-Glycerophosphate disodium salt (β-GP, G9422, Sigma-Aldrich) and 10 nM dexamethasone (D4902, Sigma-Aldrich)). After the matrix production phase, all different types of cultures were exposed to a mild decellularization protocol. First, monolayers were washed 2 times with phosphate-buffered saline without calcium and magnesium (PBS, D8537, Sigma-Aldrich), and incubated in lysis buffer (20 mM ammonia (1.05432.1011, Merk, Germany) in 0.5% (v/v) PBS-Triton X100 solution (3051.3, Carl Roth, Germany)) for 10 min at 37°C under gentle agitation. Next, monolayers were washed repeatedly with excess of PBS before complete decellularization of matrices with DNase 100 Units/mL (DN25, Sigma-Aldrich) dissolved in 0.15 M sodium chloride (NaCl, P029.3, Carl Roth) incubation for 1 h at 37°C under gentle agitation. dECM were finally washed twice with PBS and stored for no longer than 1 month at 4°C in PBS supplemented with 1% Pen/Strep until allogeneic BM-MSC seeding.

Decellularization efficiency

In order to assess the efficiency of the decellularization protocol, matrices for each condition were fixed in 4% paraformaldehyde (PFA, 11762, Morphisto, Germany) just after the matrix production phase and respectively after the complete decellularization protocol. Monolayers were washed twice with excess of PBS, followed by staining of cell nuclei with 4′,6-diamidino-2-phenylindole (DAPI, H-1200, Vectashield, USA). Coverslips were mounted on slides for fluorescence microscopy and DAPI channel images were acquired (DMi8, Leica, Germany) for each condition. Cell counting was performed with a Fiji analysis plugin (version 2.1.0/1.53f) and calculated for a total area of 1 cm^2 per sample (four region of interested selected for each technical triplicate per condition in a total of seven individual experiment).

Preparation of decellularized bone scaffolds

Decellularized bone scaffolds were obtained from human trabecular femoral head specimens (permission number: 187/18, University of Wuerzburg ethics committee), as previously described in.[25,45] Briefly, freshly thawed samples (kept at −20°C for no more than 4 months after surgery) were precisely cut in 3 mm thick slides using an electric diamond band saw (300 Exakt D64, Walter Messner, Germany) to ensure homogeneous penetration of washing solutions through the complete sample volume. Blood and residual fat material were removed by several washing cycles in water and a chloroform (288306, Sigma-Aldrich) and methanol (8388.6, Carl-Roth) mix solution. Further decalcification of bone slices was achieved by incubation for several days in 2.5% ethylenediaminetetraacetic acid (EDTA, E5134, Sigma-Aldrich) in 10 mM Tris-base (T6066, Sigma-Aldrich), from where cylindrical constructs with a diameter of 5 mm were shaped using a biopsy punch (05.SF004, Stiefel, Germany). Complete decellularization of bone samples was achieved by enzymatic treatment with 100 Units/mL DNase and finalized with lyophilization (Martin Christ, Alpha 1–2 LDplus,

Germany) for 4 days under a vacuum pressure of 1 mbar. Processed bone scaffolds were stored at −20°C. For sterilization, scaffolds were incubated with 70% ethanol 1 day before cell seeding.

Protein extraction: Electrophoresis and western-blot

For analysis of protein content in the decellularized models, matrices were collected in 1mL of RIPA buffer (89901, Thermo Fisher Scientific) supplemented with proteinase inhibitor cocktail (78440, Thermo Fisher Scientific). Homogenization of samples was performed by cycles of sonification (20×: 2 s 80% peak followed by 28 s break, Sonopus HD 4100, Bandelin, Germany) and the total amount of protein quantified using a Pierce BCA kit (23227, Thermo Fisher Scientific). Samples were reduced in the presence of 2-mercaptoethanol at 95°C for 10 min and 10 µg of total protein per condition were loaded on 10% polyacrylamide gels followed by sodium dodecyl sulfate (SDS) separation through electrophoresis (PAGE). Coomassie staining was performed for dECM characterization; enriched rat-tail Collagen-type I (C3867, Sigma-Aldrich) and FCS were run in parallel as controls. For western-blot analysis, three individual donors were used for each condition. Proteins were transferred to the nitrocellulose membrane (10600001, GE Healthcare, Germany) for 1 h and then blocked overnight at 4°C with 5% BSA in Tris (pH 8, A4577, Applichem, Germany)-buffered saline with 0.1% Tween-20 (P1379, Sigma-Aldrich). Next, membranes were incubated with primary antibodies (dilution 1:2000, Col1 (ab35710, abcam, Germany), type-VI collagen (Col6, MA5-32412, Thermo Fisher Scientific) and fetuin-A (Fet-A, homemade serum no. 5359 kindly provided by Prof. W. Jahnen-Dechent, RWTH Aachen University)) overnight at 4°C followed by incubation with secondary anti-rabbit immunoglobulin G (IgG) antibody conjugated with horseradish peroxidase (dilution 1:5000, ab205718, abcam). Finally, blots were developed by the enhanced chemiluminescence method with Chemiluminescent HRP substrate (541015, Biozym, Germany) and images acquired with the FluorChem Q imaging System (Cell Biosciences, Germany). Semi-quantification of the bands was carried out by optical densitometry and analyzed using the Fiji Gel plugin menu (version 2.1.0/1.53f). The expression of each protein is presented in relation to Col1 expression. For each protein, three independent matrices were analyzed.

Proteomics analysis: Mass spectrometry (MS)

For proteomics studies one sample for each condition was analyzed by MS. Briefly, protein precipitation was performed overnight at −20°C with 4× volume of acetone. Pellets were washed with acetone at −20°C. Precipitated proteins were dissolved in NuPAGE® LDS sample buffer (NP0007, Thermo Fisher Scientific), reduced with 50 mM DTT at 70°C for 10 min and alkylated with 120 mM iodoacetamide at room temperature for 20 min. Separation was performed on NuPAGE® Novex® 4%–12% Bis-Tris gels (NP0321PK2, Thermo Fisher Scientific) with MOPS buffer according to manufacturer's instructions. Gels were washed three times for 5 min with water and stained for 1 h with Simply Blue™ Safe Stain (LC6065, Thermo Fisher Scientific). After washing with water for 1 h, each gel lane was cut into 15 slices. The excised gel bands were destained with 30 % acetonitrile in 0.1 M NH_4HCO_3 (pH 8), shrunk with 100 % acetonitrile, and dried in a vacuum concentrator (5301, Eppendorf, Germany). Digests were performed with 0.1 µg trypsin per gel band overnight at 37°C in 0.1 M NH_4HCO_3 (pH 8). After removing the supernatant, peptides were extracted from the gel slices with 5% formic acid, and extracted peptides were pooled with the supernatant.

NanoLC-MS/MS analyses were performed on a LTQ-Orbitrap Velos Pro (Thermo Fisher Scientific) equipped with a PicoView Ion Source (New Objective) and coupled to an EASY-nLC 1000 (Thermo Fisher Scientific). Peptides were loaded on a trapping column (2 cm × 150 µm ID, PepSep) and separated on capillary columns (30 cm × 150 µm ID, PepSep, Denmark) both packed with 1.9 µm C18 ReproSil and separated with a 30 min linear gradient from 3% to 30% acetonitrile and 0.1% formic acid and a flow rate of 500 nL/min. MS scans were acquired in the Orbitrap analyzer with a resolution of 30000 at m/z 400, MS/MS scans were acquired in the Orbitrap analyzer with a resolution of 7500 at m/z 400 using HCD fragmentation with 30% normalized collision energy. A TOP5 data-dependent MS/MS method was used; dynamic exclusion was applied with a repeat count of 1 and an exclusion duration of 30 s; singly charged precursors were excluded from selection. Minimum signal threshold for precursor selection was set to 50,000. Predictive AGC was used with AGC target a value of 1e6 for MS scans and 5e4 for MS/MS scans. Lock mass option was applied for internal calibration in all runs using background ions from protonated decamethylcyclopentasiloxane (m/z 371.10124). Raw MS data files were analyzed with MaxQuant version 1.6.2.2.[46] Database search was performed with Andromeda, which is integrated in the utilized version of MaxQuant. The search was performed against the UniProt Human database. Additionally, a database containing common contaminants was used. The search was performed with tryptic cleavage specificity with three allowed miscleavages. Protein identification was under control of the false-discovery rate (1% FDR on protein and peptide level). In addition to MaxQuant default settings, the search was performed against following variable modifications: Protein N-terminal acetylation, Gln to pyro-Glu formation (N-term. Gln) and oxidation (Met). Carbamidomethyl (Cys) was set as fixed modification.

Proteins of particular interest were selected based on their involvement in the following groups: bone extracellular matrix components, intracellular and membrane proteins, and hematopoietic compartment related proteins. The intensity based absolute quantification (iBAQ) log10 transformed values calculated by the software algorithm were plotted in heatmap graphs corresponding to the molar quantities found for each protein using official gene symbols.

Scanning electron microscopy (SEM) and energy dispersive x-ray spectroscopy (EDS)

The ultrastructure of decellularized-matrices and BM-MSC morphology (initial seeding: 10^4 cells per cm^2) were evaluated for each cell-seeded model after 48 h of basal culture, that is, cultivation in standard BM-MSC expansion medium without FGF, by SEM (Crossbeam 340 with secondary electron detector, Carl Zeiss, Germany). The samples were fixed on ice for 15 min with 6% glutaraldehyde (G5882, Sigma-Aldrich), dehydrated in a serial dilution of ethanol, dried in hexamethyldisilazane (440191, Sigma-Aldrich) and stored at 4°C. Prior to imaging, all samples were sputter-coated (EM ACE600, Leica, Germany) with a 4 nm film of platinum to ensure conductivity of the sample's surface. Images were taken at an acceleration voltage equal to 2–3 kV. Cellular details were artificially colored on magnified images using Photoshop® CS6 (Adobe, v13.0.1) for visualization purposes.

Additionally, dECM models without cells were also prepared and the surface atomic composition was evaluated using energy dispersive X-ray spectroscopy with a silicon drift detector (X-MaxN 50, Oxford Instruments, United Kingdom) setting the acceleration voltage of the SEM's electron beam to 10 kV. Two random areas of interest were evaluated for each sample. Mineral distribution and composition were analyzed using AZTech (Oxford Instruments).

Immunofluorescence staining and microscopy

Immunofluorescence analysis of matrix-associated bone proteins was performed to visualize their presence and distribution in the generated dECM models. Briefly, decellularized-monolayers were fixed in 4% PFA for 15 min at 4°C followed by blocking with 1% BSA-PBS (10735086001, Roche, Germany) for 1 h at room temperature and incubation with primary antibody (anti-Col1 (sc-293182, Santacruz, Germany), anti-laminin (sc-74418, Santacruz), anti-osteopontin (sc-21742, Santacruz), 1:500 dilution in 1% BSA-PBS)) overnight at 4°C. After washing, samples were incubated with secondary antibody (dilution 1:100, goat anti-mouse IgG-FITC, sc-516140, Santacruz) for 2 h at room temperature. Finally, samples were slide-mounted for microscopy (H-1000, Vectashield, Germany) and representative pictures were acquired using a fluorescence microscope (DMi8, Leica).

To confirm expression of CXCL12 by BM-MSC seeded on decellularized models after 5 days in basal culture (initial seeding: 10^4 cells per cm^2 for dECM models and 4×10^5 cells per dBone scaffold, seeding protocol previously described in Pereira et al.[45]), immunofluorescence analysis was performed on both dECM monolayers and 12 µm cryosections of dBone scaffolds (sectioning protocol previously described in Pereira et al.[45]). Samples were fixed in 4% PFA for 15 min at 4°C and permeabilized with 0.1% (v/v) Triton-X /PBS for 30 min at room temperature. BSA-blocking was performed for 1 h before the overnight incubation with CXCL12-primary antibody (dilution 1:100, MAB350, R&D System, Germany) at 4°C. In addition, Phalloidin-iFluor 488 (dilution 1:500, ab176753, abcam) was added during primary antibody incubation for cell cytoskeleton visualization. After washing, samples were incubated with secondary antibody (dilution 1:100, goat anti-mouse IgG conjugated with Alexa Fluor® 594, ab150116, abcam) for 2 h at room temperature and embedded in mounting medium containing DAPI for nuclei staining. For all stainings, secondary antibody specificity controls were performed by executing the full protocol for each sample in the absence of primary antibody.

Cell shape analysis

For BM-MSC morphology analysis, cells were seeded on dECM matrices at a density of 10^4 cells per cm^2 for 48 h in basal culture and then fixed with 4% PFA for 15 min. Cell and nuclear morphology were assessed using phalloidin and DAPI staining respectively, as previously described. Automated quantification of cellular shape features was performed using CellProfiler[47] (version 4.0.6, pipeline description in Supplemental Figure S1). Selection of poorly thresholded cells or overlapping parts was performed by unique numbering of individual segmented cells exported to the spreadsheet. At least 350 cells were assessed for each experimental group, with approximately equal numbers of cells analyzed from each of seven independent experiments. Overall morphological signatures were constructed for each group using nine cellular descriptive features (form factor, eccentricity, area, solidity, perimeter, aspect ratio, extent, orientation, compactness, area, aspect ratio, and compactness).

Separate principal component analysis (PCA) was performed using single-cell morphological data (200 cells presented in density plots of PC space) using all available CellProfiler data given for four independent experiments. Representative cells were chosen randomly from the centroids for each condition. Statistical significance of each significant parameter was evaluated with the mean value corresponding to each independent run for a total of seven experiments.

Alizarin-red staining

Matrix-mineral deposition was measured by Alizarin-red staining and subsequent quantification, according to standard protocols. To test the effect of the decellularization protocol, analysis was performed before and after decellularization for each dECM model. In addition, we assessed the osteogenic differentiation potential of seeded BM-MSC (initial seeding: 2×10^4 cells per cm^2) after 21 days in osteogenic medium (DMEM low glucose medium supplemented with 10% FCS, 1% Pen/Strep, 1% HEPES, 50 µg/mL ASC, 5 mM β-GP and 10 nM dexamethasone) or control conditions (osteogenic medium without differentiation factors). Briefly, at the analysis timepoint cells were washed twice with cold PBS and fixed in 70% ethanol (T913.3, Carl Roth) for 1 h at −20°C. Monolayers were allowed to air-dry and mineral deposition was stained with 2% Alizarin-red solution (0223, ScienCell, USA) for 15 min at room temperature under gentle agitation. After repeated washing steps, representative images were taken, followed by absorbance quantification of the resulting staining. Staining was eluted in 10% cetylpyridinium chloride (C0732, Sigma-Aldrich) solution for 20 min under gentle agitation. Absorbance of samples and standard were measured (infinite M200, Tecan, Switzerland) in a 96-well plate at 570 nm in duplicates. Results were calculated as mM (or µg/mL) of Alizarin-red. Technical triplicates were analyzed for nine individual experiments.

Resazurin viability assay

Cell metabolic activity of BM-MSC seeded on different decellularized models was assessed over a total period of 10 days in basal culture (initial seeding: 10^4 cells per cm^2 for dECM models and 4×10^5 cells per dBone scaffold) with a resazurin reduction assay. Briefly, at day 0 (4 h after seeding), 2, 5, and 10 BM-MSC seeded on each model were incubated with 10% sterile solution of resazurin (R7017, Sigma-Aldrich) in cell culture medium. The reduction assay was performed for 4 h, followed by fluorescence reading of metabolized resazurin-product at 560 nm emission/590 nm absorption wavelengths. Measurements were normalized with blank (no cells) and for each model controls without cells were tested in parallel to confirm their respective biologic inertness. Technical triplicates were analyzed for three individual experiments.

Flow cytometry

For quantification of cell viability and analysis of cell cycle stage, BM-MSC (initial seeding: 10^4 cells per cm^2 for dECM models and 4×10^5 cells per dBone scaffold) cultured on decellularized models were collected by trypsinization for 20 min at 37°C under strong agitation, and pooled (six wells for each dECM model and two dBone scaffolds) for flow cytometry staining. Cells were washed twice in PBS and incubated with Fixable Viability Dye eFluor™ 780 (65-0865-14, Thermo Fisher Scientific) for 30 min at 4°C in the dark according to manufactures recommendations, followed by repeated washing in 1% FCS-PBS. To detect cells entering different apoptotic stages, cells were then prepared and stained with fluorochrome-conjugated Annexin V (A35111, Thermo Fisher Scientific) for 15 min at room temperature. Finally, cells were fixed with 2% PFA for 15 min at 4°C and stained with 10 µg/mL DAPI solution in 1% FCS-PBS for DNA amount detection. Samples were analyzed at the Attune NxT Flow Cytometer (Thermo Fisher Scientific) and data evaluated using the software FlowJo (version 10.5.3). Six individual experiments were tested.

Real-time quantitative polymerase chain reaction (PCR)

To analyze early gene expression response of BM-MSC to the decellularized models, cells from six 13 mm wells or two scaffolds were pooled together for RNA harvesting in Tri-Reagent (T9424, Sigma- Aldrich) after 5 days in basal culture (initial seeding: 10^4 cells per cm^2 for dECM models and 4×10^5 cells per dBone scaffold). BM-MSC cultured on coverslips were used as controls. Homogenization and cell lysis were performed by mechanical disruption for 5 min at 50 Hz (TissueLyser LT, Qiagen, Germany). Samples were stored at −80°C until further processing. RNA was isolated by 1-bromo-3- chloropropane (B9673, Sigma- Aldrich) phase separation followed by column separation according to the manufacturer's instructions (NucleoSpin RNA, Macherey-Nagel, Germany). cDNA was synthesized by reverse transcription (Oligo (dT) C110A, dNTP Mix U151A, M-MLV RT 5× Buffer M531A, and M-MLV Reverse Transcriptase M1708, Promega, Germany) from 1 µg of RNA. Real-time PCR was performed by CFX96 Real-Time System (1845096, Bio-Rad, Germany) using SYBR Green dye (GoTaq® qPCR Master Mix, A600A, Promega) following a standardized program: 2 min at 95°C, 45× (30 s at 95°C and 1 min at 60°C), melting curve at 65°C–95°C. Primers for stem marker genes (nestin and octamer-binding transcription factor 4 (Oct4)) and genes related with niche-microenvironment (Survivin and C-X-C Motif Chemokine Ligand 12 (CXCL12)), and osteogenesis (RUNX Family Transcription Factor 2 (Runx2), alkaline phosphatase (ALP), Col1 and secreted phosphoprotein 1/osteopontin (SPP1)) were designed in the Primer Blast tool from NBCI and purchased from Biomers.net (Germany). Primer sequences and NCBI reference numbers appear in Supplementary Table S1. Expression of target genes was normalized with beta-2-microglobulin (B2M) as the reference gene, and results displayed as relative values ($10^4 \times 2^{-\Delta Ct}$).

Statistical analysis

Quantitative data was analyzed using Graphpad Prism software (version 9.1) and presented as the mean ± standard error of the mean. Statistical significance was generally determined using the Kruskal–Wallis method followed by Dunn's multiple comparisons test. Statistical significance was set to $p < 0.05$. *n* refers to number of BM-MSC donors independently tested.

Results and discussion

Preparation and characterization of 2D dECM models

Here, we generated 2D dECM in vitro models by inducing human BM-MSC to synthesize and secrete de novo ECM proteins during a total time of 10 or 21 days, in presence of osteogenic differentiation medium (O-matrix) or in basal medium supplemented with ASC (B-matrix), followed by a mild decellularization protocol (Figure 1(a)). Based on previously published work on cell culture-derived ECM as cell niche models,[48–50] we hypothesized that by controlling the cell culture environment, we would be able to trigger synthesis of ECM key components necessary to either influence differentiation[51] or preserve BM-MSC's stemness properties.[52] Numerous decellularization protocols for virtual all types of tissues and in vitro systems have been described, although no standard criteria have yet been defined. Generally, the protocols involve a combination of physical, chemical, and enzymatic techniques tailored to balance the preservation of unique physical and biochemical properties, and the complete removal of cellular and antigen epitopes material.[33,40] In this study, we first optimized the decellularization protocol considering each matrix (data not shown). The selected protocol involved treatment of cell-monolayers with a sequential series of short incubations in Triton X-100 and ammonia to disrupt the cell membranes and lyse the cells, followed by slow DNase enzymatic removal of remaining nuclear material alongside with continuous gentle agitation. DAPI staining of the matrices (Figure 1(b)) showed efficient removal of cells and nuclei for all conditions after the decellularization protocol, resulting in a residual average of 2.8 nuclei counted per cm^2 compared to 127.6 before. Considering that the whole process of decellularization naturally disrupts the ECM to some extent,[53] we then examined the structure and biochemical composition of the resulting dECM matrices. We observed presence of homogenously distributed fibrillar type-I collagen (Col1) in all decellularized matrices (Figure 1(d)). Col1 is the most abundant extracellular protein in bone and plays a fundamental role in the structure and mechanical strength of the tissue.[54,55] Therefore, we decided to supplement the basal control cultures with ASC to generate a collagen-rich ECM as well.[56] Bone-specific ECM proteins[57] such as laminin and osteopontin, on the contrary, have been only detected with a spotted distribution in the 21-day decellularized osteogenic matrix (O21). Similarly, Coomassie stained SDS-PAGE (Figure 1(c)) revealed a strong band at 138 kDa and 129 kDa for all matrices, most likely accounting for presence of Col1 α1 and α2-chains, respectively, as indicated by the purified Col1a control. Not surprisingly, these matrices also exhibited presence of bands (67 kDa) that can be speculated to be associated with albumin derived from cell culture FCS. Other observed bands are conjectured to be associated with highly-concentrated categorical-ECM proteins, for example, fibronectin (262 kDa), laminin (177 kDa), elastin (68 kDa), osteonectin (34 kDa), osteopontin (32 kDa), etc. Nonetheless, each matrix shows an overall complex and unique protein pattern, similar to what has been reported in literature,[48,58] and further assessed in the present study by MS. Lastly, we explored the effect of the decellularization protocol on the mineralization residues of the produced matrices.

Quantification of Alizarin-red dye (Supplemental Figure S2) for all conditions showed a general decrease of mineral content after decellularization. Particularly, O21 matrices showed a high concentration of mineral residues before decellularization, however EDS analysis (Supplemental Figure S3) revealed no detectable presence of minerals, such as calcium and magnesium, after decellularization.

Effect of dECM models on BM-MSC's osteogenic potential

Cellular morphology has traditionally been considered as an important qualitative indicator of cell behavior and state. Interestingly, while changes in cell shape are associated with descriptive traits of specific biology processes, studies have shown that cell shape in turn plays an important role in regulating cell fate, emerging as a fine bond between the interplay of physics and cell biology.[59,60]

In order to assess the effect of dECM substrates on cell behavior, we first analyzed cell morphology of seeded BM-MSC after 2 days of culture by SEM (Figure 2(a)). Cells seeded on coverslips (CS) were used as controls. CS-cultured cells displayed a widespread morphology. In contrast, cells on dECM seem to have acquired an explicit orientation and rather favor cell-ECM interactions. High-magnification images reveal the complexity of BM-MSC (colored in blue) interactions with the fibrous-collagen rich dECM substrates through numerous cytoplasmic extensions, which corroborates the functionality and relevance of the dECM models. In fact, the morphology of a cell is known to be primarily determined by a combination of physical and biochemical interactions with its surrounding ECM, reflecting an integrative effect across a wide range of multiple processes and signaling pathways, such as migration,[61,62] lineage commitment,[63–65] function or dysfunction[66] and cancer progression.[67] Therefore, monitoring cellular morphology has also been used as a practical and non-invasive approach to predict lineage commitment of

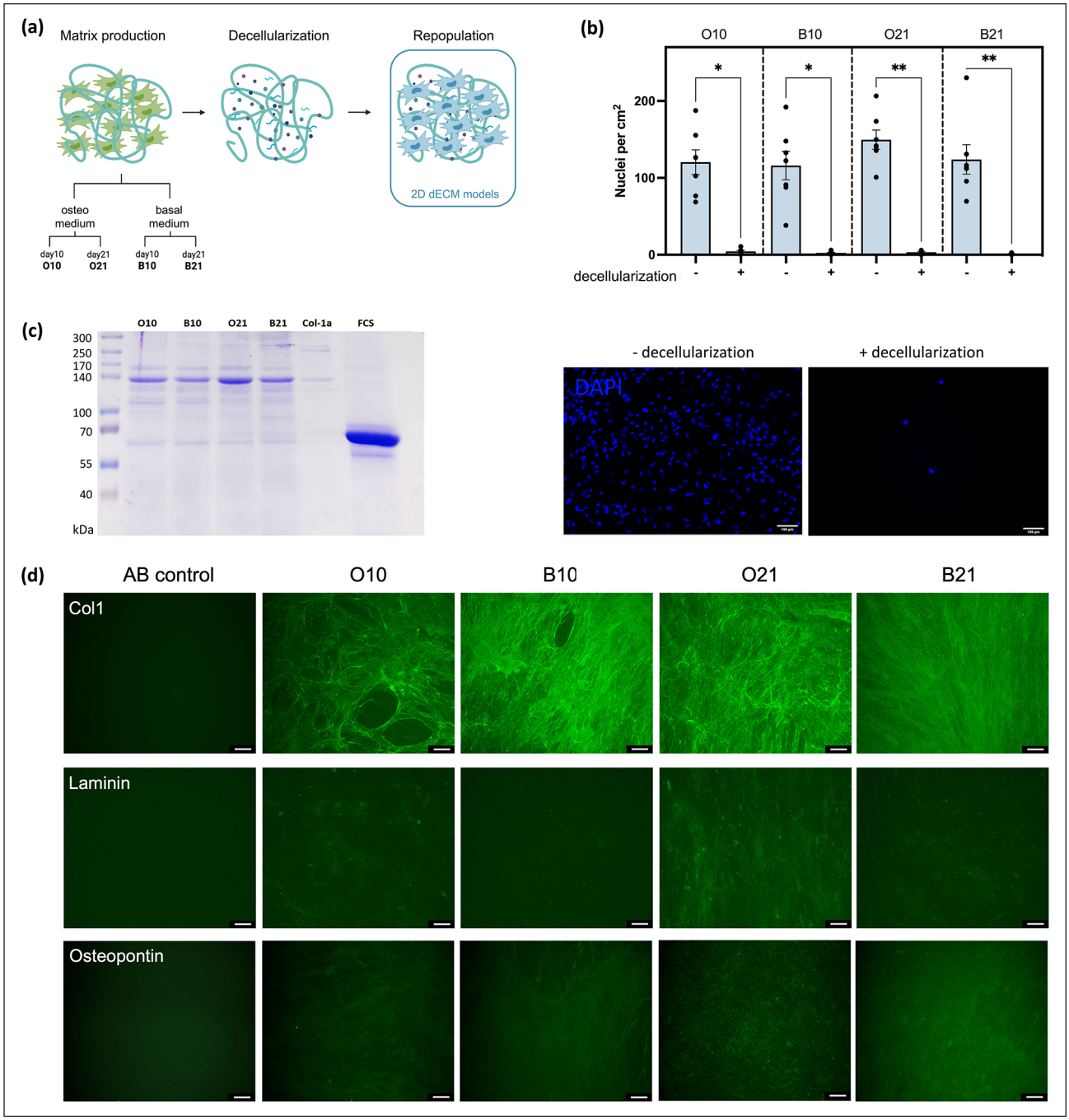

Figure 1. Production and characterization of BM-MSC-derived 2D dECM: (a) Schematic protocol of the development of dECM models. The first phase involves the key period of synthesis and secretion of ECM proteins by BM-MSC, where unique stimuli target the production of specific environments. Next, monolayers are treated by a multi-step decellularization protocol, therefore eliminating any nuclear material yet retaining the biochemical and structural complexity of the previously produced matrices. Finally, the last step is the repopulation of the dECM models and the study of the differential behavior of BM-MSC seeded on each matrix. Images created with BioRender.com. (b) Decellularization efficiency analysis. ECM-cell monolayers were fixed before and after the decellularization protocol and cell nuclei stained with DAPI. Quantitative and qualitative (representative images) analysis was performed, confirming the efficient decellularization protocol for all types of matrices. (Statistic: Kruskal–Wallis one-way test, $*p < 0.05$, $n = 7$). (c) Coomassie stained SDS-PAGE of collected matrices in reduction conditions. Rat-tail derived Col1 concentrated solution and FCS were used as control in order to identify specific bands in the samples. Total protein loaded per well 10 μg. (d) Immunofluorescence staining of bone-ECM proteins (Col1, laminin and osteopontin). Absence of detectable signal in secondary antibody (AB) controls (left column) confirms that they do not bind unspecifically to matrix-associated proteins, therefore validating the positive signal detected in presence of each individual antibody. Acquired FITC-colored images are shown. Scale bar: 100 μm.

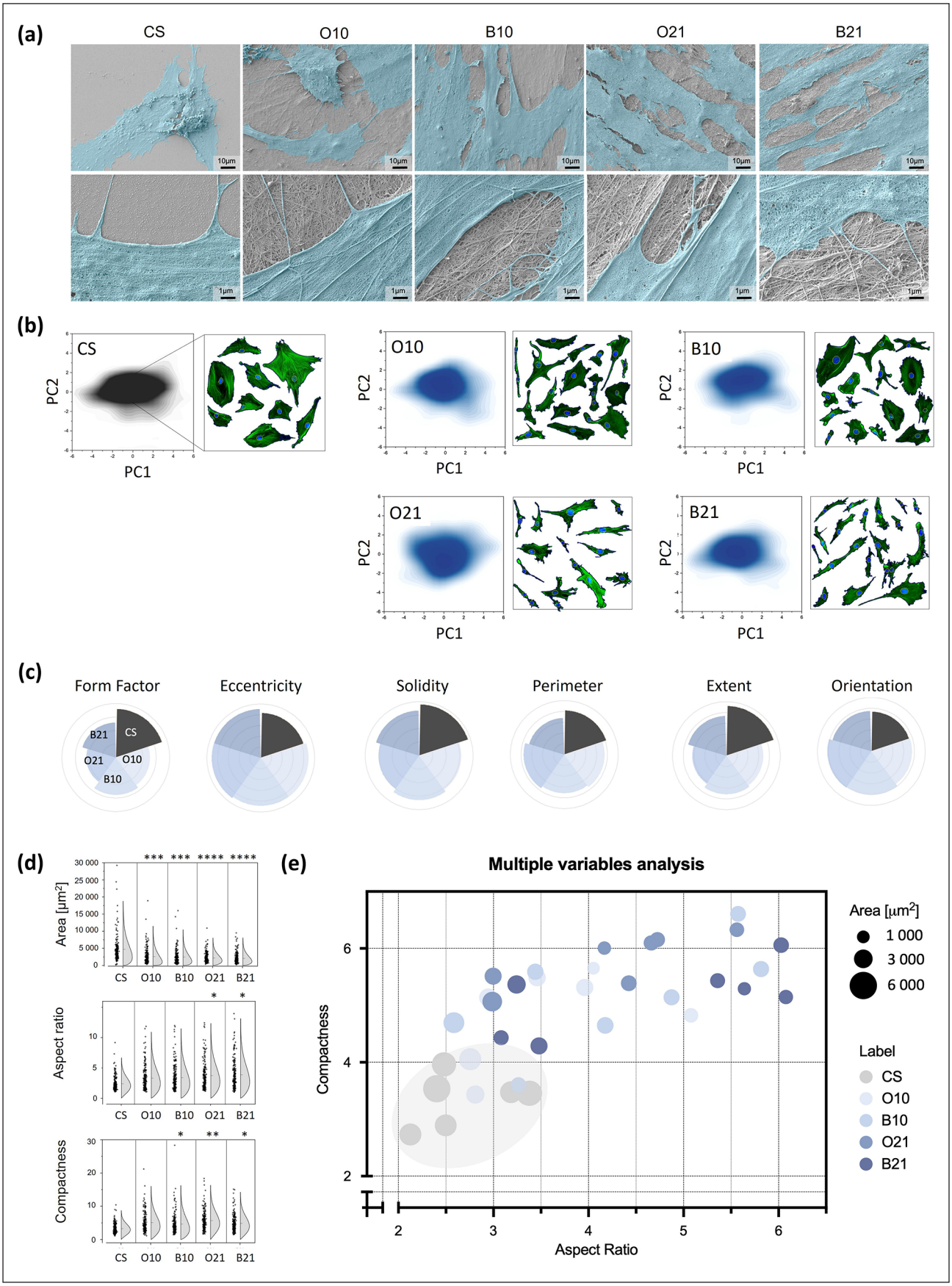

Figure 2. *(Continued)*

Figure 2. Cell shape analysis of human BM-MSC cultured on dECM for 2 days: (a) Representative SEM images of BM-MSC`s early morphological response to the culture substrate. For visualization purposes the cell surface was artificially colored in blue with Photoshop. Low magnification images (first row) uncover the overall cell shape morphology of BM-MSC on each culture substrate, where a clear elongation and orientation is enforced on dECM cultured BM-MSC, particularly on O21 and B21 matrices. Scale bar: 10 μm. High magnification images (bottom row) illustrate single cell interactions with the ECM through cytoplasmic extensions. A highly complex fibrous collagen-like matrix is detected for all dECM models. Scale bar: 1 μm. (b) Principal-component (PC) analysis from single-cell morphological data of fluorescently labeled cells (β-actin and DAPI staining) ($n = 200$ total points per condition, collected from four individual experiments). PC1 accounted for 44%–47% of the data variance. Representative segmented boundaries, exported from CellProfiler pipeline, are illustrated (right column) for each condition as qualitative evidence. (c) Substrate-specific cell shape descriptor variance. Pie-charts corresponding to the variance of six non-significantly different shape-parameters exported from the CellProfiler pipeline (form factor, eccentricity, solidity, perimeter, extent, and orientation, $n = 200$ from four individual experiments). (d) Normal distribution and statistical analysis of the three significant shape-parameters selected (area, aspect ratio and compactness, repeated measures (RM) one-way ANOVA, $*p < 0.05$, $**p < 0.01$, $***p < 0.001$, $****p < 0.0001$, $n = 350$ from seven individual experiments). (e) Three-dimensional multiple variable analysis showing connection between the top three morphological features: area (symbol size), aspect ratio (x-axis), and compactness (y-axis) with the BM-MSC culture substrate (color map shown on the right of the graph, $n = 350$ from seven individual experiments).

stem cells. While these assessments have historically been applied qualitatively and require experienced interpretation, recently high-throughput single-cell bioimaging has enabled quantification of numerous shape descriptors from a heterogeneous cell population. Particularly, Marklein et al.[68] demonstrated the prediction of BM-MSC mineralization at day 35 from several human donors, based on automated morphometric descriptor analysis at day 3 of osteogenic induction with over 90% accuracy.

Here, we developed a robust protocol (pipeline in Supplemental Figure S1) for automated high-throughput quantification of cell shape descriptors, based on fluorescent-labeled cytoskeletal images of seeded BM-MSC on dECM matrices after 2 days of culture. Supporting the cell morphology observations in SEM, the integration of the multi-parametric acquired features into a principal-component analysis (Figure 2(b)) revelated a clear segmentation of matrix-seeded BM-MSC when compared to the tissue culture plastic control, both by qualitative observation of segmented single-cell images and by quantitative analysis of cell shape descriptors. With the purpose of obtaining reliable and biological significant results,[69] from nine shape descriptors acquired (form factor, eccentricity, area, solidity, perimeter, aspect ratio, extent, orientation, and compactness, Figure 2(c)), three significant parameters (area, aspect ratio and compactness) were selected, considering both their definition and interpretation, for further analysis (Figure 2(d)). In fact, due to the combined results of these three parameters, individual clusters could be identified in a 3D graph of multiple variables (Figure 2(e)). Control CS-seeded BM-MSC are categorically bigger in size (area $>4000\,\mu m^2$) and display a rather simple (i.e. low compact values, restricted to its spatial boundaries) and spherical shape (aspect ratio values closer to 1). In opposite, cells seeded on dECM models, particular day 21-matrices (O21 and B21), reveal an evident shift from the CS cluster in all three dimensions — cell size/area is significantly reduced, while cells exhibit a rather elliptical and complex shape, creating a state of cytoskeletal tension, characteristic of a pre-osteogenic differentiation phenotype.[70]

Previous literature has shown that osteogenic lineage determination occurs within the cell cytoskeleton itself, that is, adhesion protein complexes communicate the cell tension state to the cell nucleus via mechanotransducive cascade involving yes-associated protein 1 (YAP)/transcriptional coactivator with PDZ-binding motif (TAZ), leading to the activation of RhoA-associated signaling pathways, therefore specifically promoting the osteogenic differentiation process.[63,71]

Thus, we further compared the osteogenic potential of BM-MSC seeded on dECM in presence and absence of osteogenic factors, that is, ASC, dexamethasone and β-GP, by means of mineral deposition at day 21 (Figure 3). Interestingly, there was no apparent effect on differentiation of BM-MSC (red bars) when cultured on different substrates, with observed mineral deposition for all conditions. Yet, BM-MSC cultured on dECM models in absence of external differentiation factors (white bars) show a trend toward an increased mineral deposition in comparison to CS control cultures, particularly significant for the O21 condition. Furthermore, an increased number of competent colony-forming cells in the dECM models was observed in comparison with CS control cultures, advocating for the superior supportive-effect of decellularized ECM models as a culture substrate for BM-MSC expansion (Supplemental Figure S4). It seems that BM-MSC interaction with dECM topography- and chemical-associated features governs the initial cell adhesion, resulting in a stronger intercellular connectivity in the early phase of cell culture. It follows from this that enhanced cell-cell contacts accelerate the osteogenic differentiation cascade.[72] Hence, these findings validate the cell-shape prediction results, which shows to be in line with a common organogenesis theory hypothesizing that cellular function may indeed follow form.[73]

Notwithstanding, BM-MSC lineage fate decision is a complex process influenced by several microenvironmental factors; whilst topography imposes a physical constraint to cells and ultimately to tissue structure (in a process known as mechanotransduction),[74] integrin-matrix

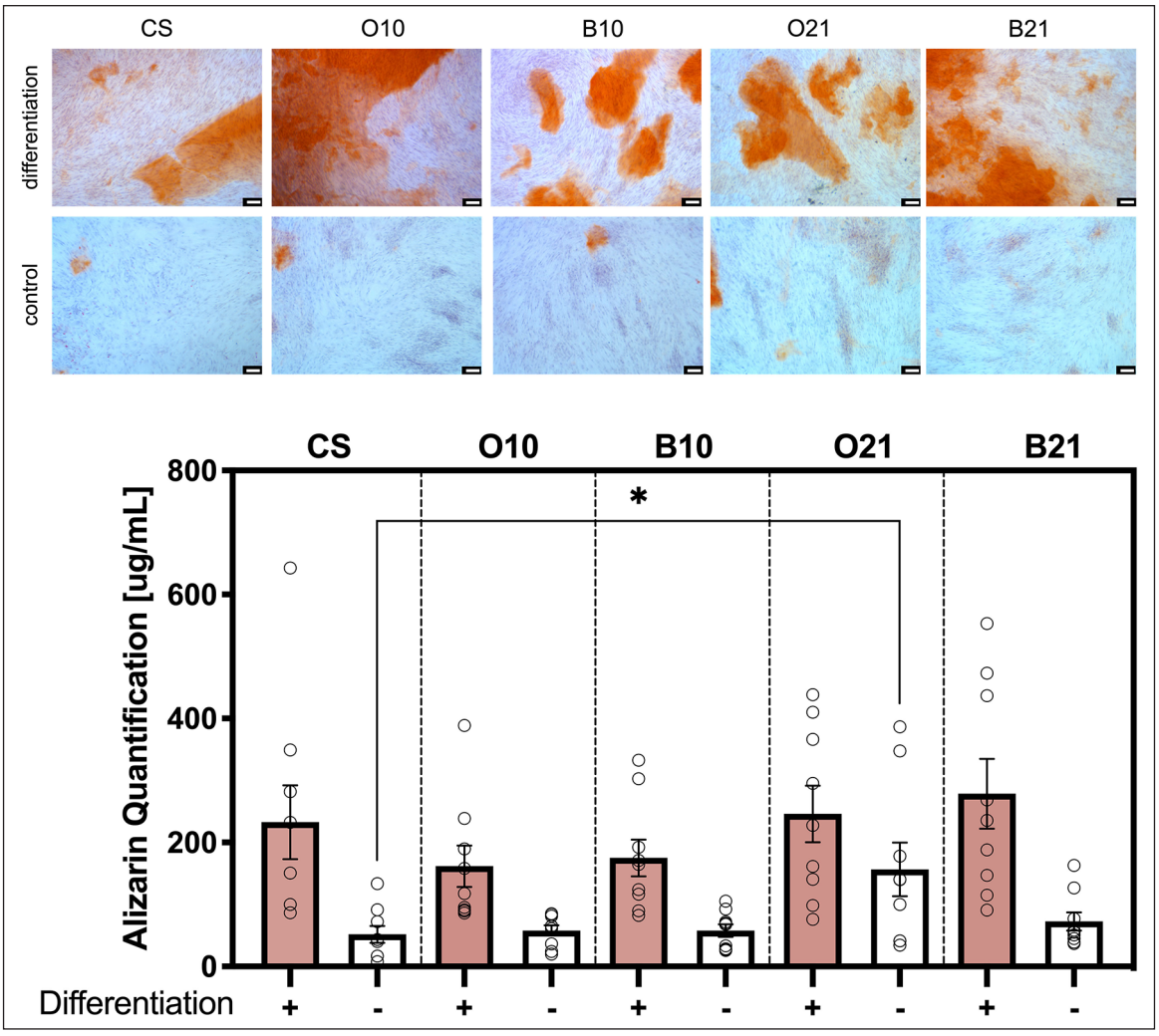

Figure 3. Human BM-MSC's osteogenic potential assessed by mineral deposition analysis at day 21. Representative images of Alizarin Red S staining at day 21 of osteogenic culture (top panel). Osteogenic differentiation was stimulated by supplementation of low-glucose cell culture medium with osteogenic factors (i.e. ASC, dexamethasone, and β-GP). Control cultures for each substrate were performed in parallel in absence of osteogenic-inducing factors. Scale bar: 100 μm. Quantification of Alizarin Red S staining (bottom panel) shows no effect of dECM on BM-MSC mineralization in presence of differentiation-inducing medium (red bars). Although in absence of external differentiation factors (white bars), a significant increase of mineral deposition of BM-MSC seeded on O21 matrix was detected when compared with cells cultured in the same conditions on CS substrate (two-way ANOVA multiple comparisons, $*p < 0.05$, $n = 9$).

interactions likewise play a pivotal role in gene expression, phenotype, and eventually cell fate by direct signal transducing to the nucleus. In contrast to the artificial overimposing chemically-induced osteogenic differentiation methods, commonly applied in research, dECM models seem to provide a rather natural substrate for BM-MSC expansion, while specific features on ECM osteogenic-produced matrices are able to trigger spontaneous osteogenic differentiation of BM-MSC.

dECM and dBone comparative chemical-composition analysis

As the native niche develops, most of the local microenvironmental cues are highly heterogeneous and continuously dynamic over time. The complexity of this process imposes difficulties in uncovering the role of individual features of well-defined ECM properties and signals in cellular responses. Several biomaterials have been designed to capture key molecular cues that mimic particular aspects of the natural extracellular milieu, such as mechanical properties, structural characteristics, chemical composition, and bioactive compounds[75,76]; however, they still represent a rather simplistic approach to the full complexity of the tissue. Therefore, full tissue decellularization techniques appear as a straightforward method to retain the physical and chemical complexity of the naïve environment. We have previously established a human decellularized trabecular bone 3D scaffold (dBone, dB), proved to be a suitable in vitro model to study the complexity of the

bone skeletal environment.[45] We speculate that beyond the dimensionality, specific protein expression patterns in cell-based and bone-derived decellularized models might play a significant role in BM-MSC in vitro cell fate.

Thus, here we conducted a comparative investigation considering the chemical composition and subsequent behavioral differences of cells interacting with both dECM and dBone models.

To this end, MS-based high-throughput proteomics techniques provide a feasible exploratory approach toward the identification of important bone factors that might be absent in certain models and therefore not fully reflecting the naïve environment. LC-MS detected a total of 735 proteins identified in at least one of the samples (excluding contaminants). Of these, 128 proteins were found in both dECM and 3D dBone proteome, indicating high homology of obtained dECM models to the in vivo bone niche.[77] This homology is found to particularly be evident for intracellular and membrane proteins. Interestingly, we found by gene ontology (GO) analysis (Figure 4(a)) that there were proteins specifically enriched in the dBone scaffold. These differentially expressed proteins were associated with bone matrix structure and metabolism, for example, secreted phosphoprotein 24 (SPP2), α2-HS-glycoprotein (AHSG) also referred to as fetuin-A; while intracellular proteins were rather enriched in dECM matrices, for example, tubulin (TUB), actin (ACT) and laminin (LMNA), recapping the cell lysis during the decellularization protocol, which has been documented likewise in other studies.[78] Moreover, further GO analysis of biological processes revealed singular expression of proteins associated with the hematopoietic compartment function, such as immune effector process and antimicrobial humoral response, for example, proteoglycans (PRG), hemoglobin (HBB), and F2 (prothrombin), specifically in dBone but not dECM, resembling the native-complexity of dBone scaffolds. Col1 accounts for nearly 95% of the entire collagen amount in the organic bone matrix and about 80% of the total proteins present in bone, playing a substantial role in the mechanical properties of the tissue, particularly for its toughness (i.e. the ability to absorb energy before rupturing).[79] Therefore, the consistent expression of Col1 throughout all models was confirmed by Western Blot analysis for three independent donors (Figure 4(b)).

The observation of an obvious band at the 138 kDa mark for all conditions confirmed the anticipated presence of a collagen-rich matrix, therefore validating the proteomic results. We were further interested in exploring expression patterns of differentially enriched proteins in different models, that is, Col6 only be detectable in dECM samples and FetA exclusively detected in dBone scaffold. Col1 basal expression was used to normalize the quantification of Col6 and Fet-A, in the samples (Figure 4(c)). Interestingly, we observed a very strong expression of Col6 (108 and 134.7 kDa) in dECM, particularly for day-21 matrices, whereas the detection in dBone samples was significantly reduced, evident for both proteomics and western blot analysis. Col6 is a nonfibrillar collagen commonly associated with ECM remodeling, specifically important in processes such as wound healing[80] and cancer progression.[81] Altogether, we postulate that stronger expression of Col6 specifically in dECM models may be a result of artificial in vitro culture, which may affect BM-MSC behavior, particularly cell motility and spreading.[82] Likewise, the detection of analogous patterns of Col14 expression may be postulated as an in vitro artifact as well. Col14 has been known as regulator of fibrillogenesis,[83] and is often present in areas of high tissue mechanical stress,[84] advocating toward the aforementioned artificial excessive ECM remodeling in in vitro culture. We further found an enrichment in dECM models of proteins involved in ECM-cell binding and other cellular responses, for example, transforming growth factor beta (TGF-β)[85] and fibulin 2 (FBLN2).[86] The concentrations of these proteins in the dBone sample ranged below the detection limits of the technique. In fact, TGF-β was proposed to induce early stages of osteoinduction in vitro[87], therefore these results reveal the potential of dECM as a versatile tool to be used as a model where a higher exposition to growth factors is desired. On the other hand, although there is limited literature describing the isolation of in vitro cell-produced ECM and its proteomic analysis,[88,89] ECM-associated proteins selectively expressed in dBone but not in dECM models may be extremely significant to identify novel targets involved in bone-niche processes. In particular, fetuin-A (55 kDa), is one of the most abundant non-collagenous proteins found in mineralized bone. Primarily produced in the liver, fetuin-A binds to hydroxyapatite minerals in bone matrix and acts as a potent inhibitor of ectopic mineralization.[90,91] Despite its' affinity to bind to TGF-β/BMP receptors blocking osteogenic signaling, fetuin-A may also sequester cytokines in the matrix, thereby generating a reservoir of osteoinductive activity when released.[92] Similarly to fetuin-A, secreted phosphoprotein–24 (SPP2) is a liver-derived precursor of pro-osteogenic proteins, playing an important role in the rate and magnitude of BMP2-dependent bone formation.[93] Collectively, the acquired data highlight that, although structurally important proteins for cell adhesion and proliferation such as Col1 are present on both dECM and dBone models, extracellular proteins importantly involved in the bioactivity of the bone mineral phase are not detected in manufactured dECM models, due to their peripheral synthesis followed by bloodstream-transportation to the bone, which may well have an implication on the functionality of those models.

BM-MSC behavior and transcriptional activity on decellularized models

In order to study the effect of the here developed decellularized models on BM-MSC behavior, we first looked at

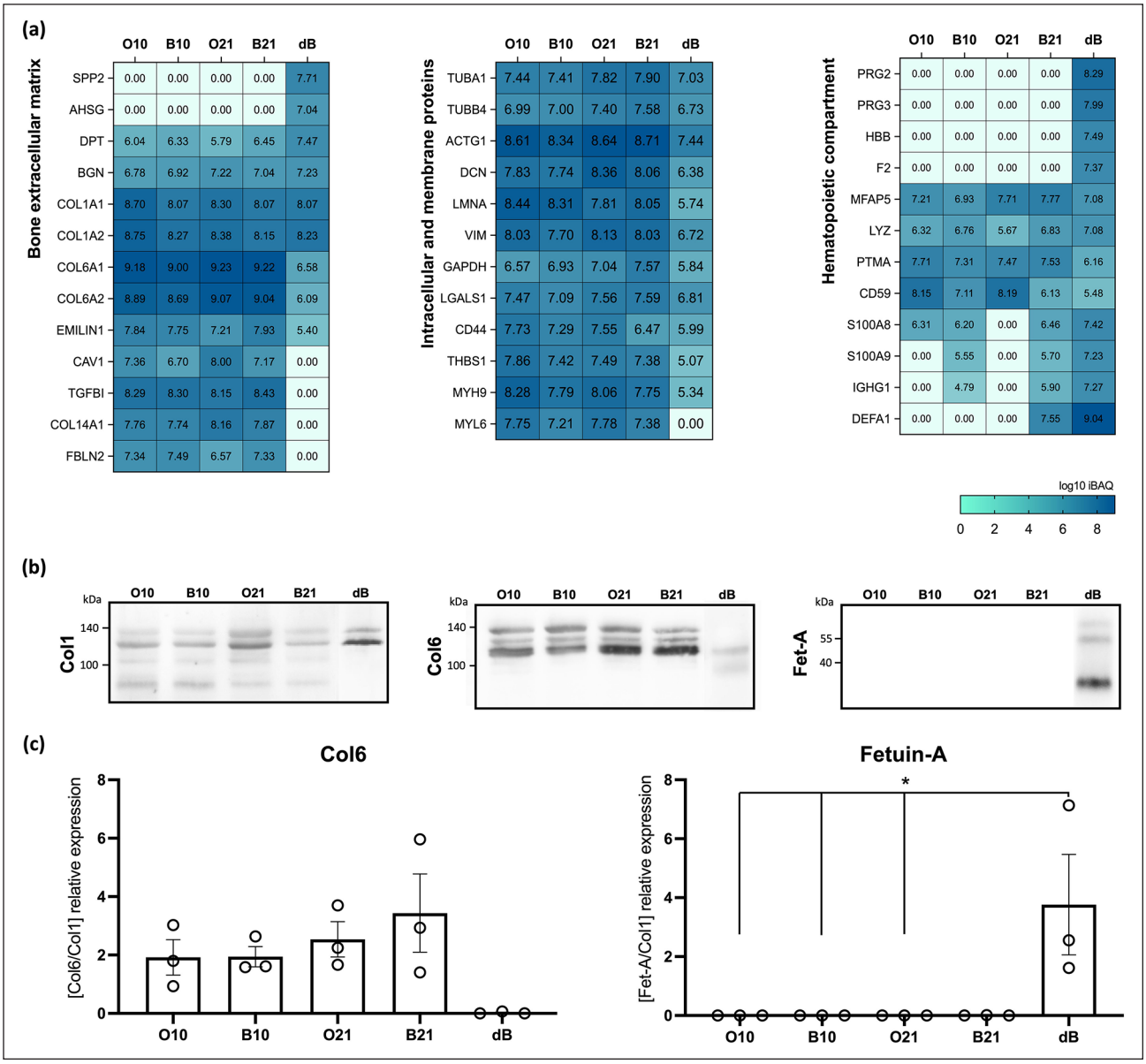

Figure 4. Proteomic analysis of collected dECM and dBone samples: (a) SDS-PAGE was performed under reduction conditions and followed by MS analysis ($n = 1$). Heatmaps show the log10 value of the relative abundance of proteins in the decellularized models (iBAQ calculated by MaxQuant). Detected proteins of interest were grouped under three main groups (bone extracellular matrix, intracellular and membrane proteins and hematopoietic compartment), showing different patterns of expression across each model (gradient blue color code). (b) Western blot analyses from electrophoresis gel separation (9 µg of total protein), of three proteins (Col1, Col6, and Fet-A), validating proteomics results (representative image of three replicates). (c) Relative quantifications of Col6 and Fet-A Western blot band expression normalized to the respective expression of Col1. Quantification of band area was performed in ImageJ using the Analyze Gel plugin (two-way ANOVA multiple comparisons, $^*p < 0.05$, $n = 3$).

cell metabolism over a period of 10 days in basal culture conditions (Figure 5(a)). In order to revalidate the metabolic inertness of the models per se, the signal of constructs without cells for all conditions and timepoints was assessed. The observed near-zero values with insignificant small variance confirm the abovementioned success of the decellularization protocol. Human BM-MSC seeded on the decellularized models were compared with control cultures on coverslip (CS). Generally, a positive and sustained increase of cell metabolic activity over time was observed in all conditions, verifying once more the cytocompatibility of the models. Moreover, the superior initial (day 0) metabolic values observed for cells seeded in the decellularized models in comparison with CS controls, confirm the previously claimed extraordinary cell adhesion facilitated by the ECM-associated features. For 3D matrices, the initial cell number was adapted to the total scaffold volume in order to achieve an equivalent confluent cell

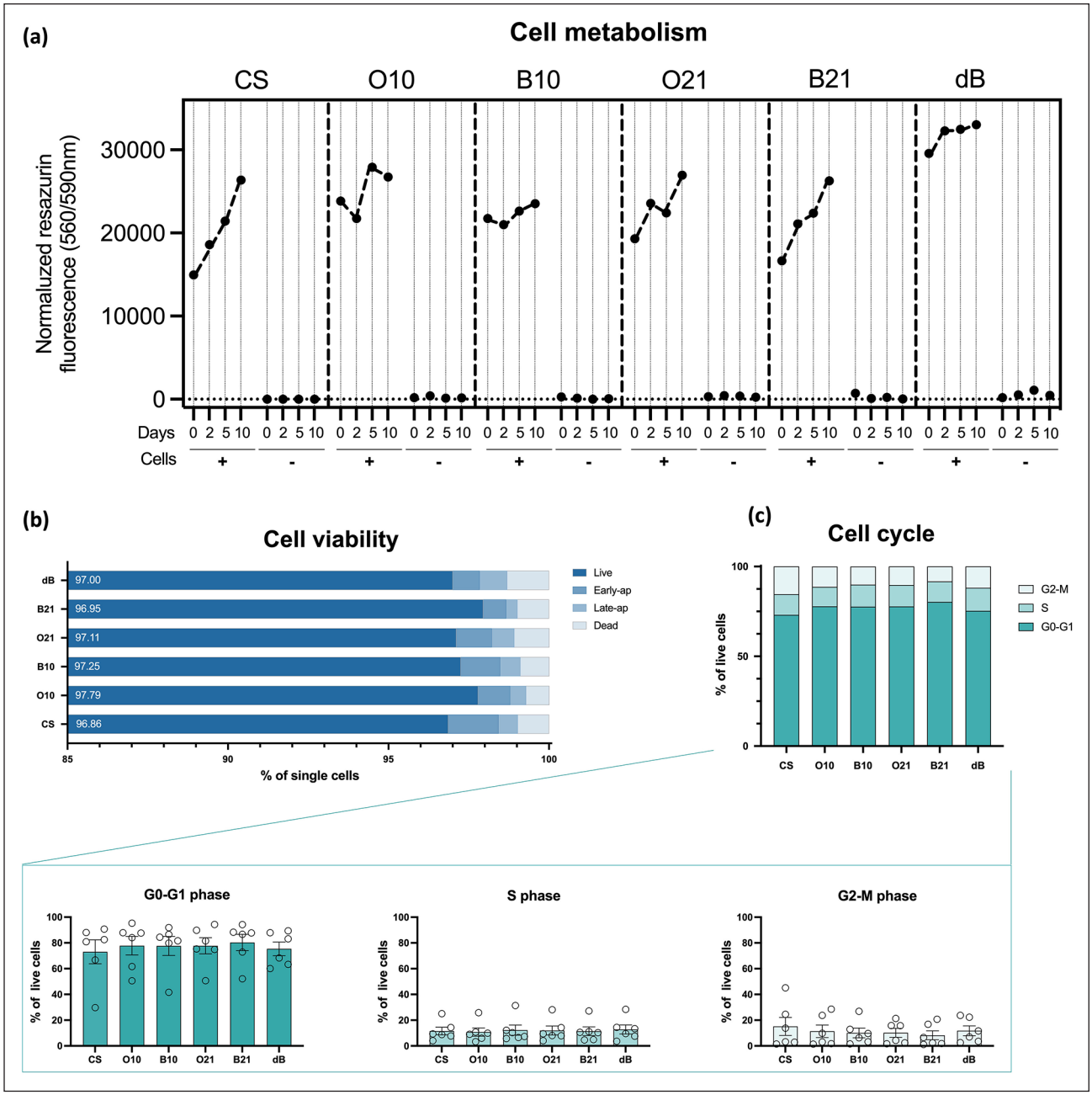

Figure 5. Analysis of metabolic activity of BM-MSC seeded on dECM and dBone models during early timepoints: (a) Metabolic analysis of BM-MSC in basal culture over time (0–10 days) measured by resazurin reduction assay shows a stable and sustained growth of BM-MSC in all models. Values were normalized with blank measurements (10% resazurin solution in cell culture medium). For each condition controls without cells were tested to prove the inert activity of decellularized models ($n = 3$). (b) Flow cytometry analysis of BM-MSC viability at day 5 of culture in decellularized models. BM-MSC in all conditions show similar results to CS control samples with live cells percentage values consistently higher than 98% ($n = 6$). (c) BM-MSC cell cycle stage analysis performed by flow cytometry based of DAPI-DNA labeled histograms. Upper panel displays the cumulative cell percentage quantification for each condition, whereas in the bottom panel individual values are displayed for enhanced visualization and interpretation ($n = 6$).

density (previously described in Pereira et al.[45]), which explains the elevated baseline signal in the dBone model. Subsequently, we took particular interest in assessing further biological changes in BM-MSC after 5 days in basal culture. Cell viability was quantified by flow cytometry of labeled cells with Annexin-V and viability dye, and live, early apoptotic, late apoptotic, or dead populations were identified (Figure 5(b)).

As anticipated from the resazurin assay results, a high percentage of viable cells was observed for all conditions, with the percentage of the live population being consistently higher than 98%. Analysis of the cell cycle stage was performed on the population of live cells, based on measurement of cellular DNA content, albeit no significant changes were observed.

In order to further investigate the hypothesized niche-phenotype of BM-MSC in the different decellularized models, we performed an extensive analysis of gene markers associated with different BM-MSC features (Figure 6(b)). In order to assess the early response of BM-MSC to the microenvironmental cues, this analysis was performed after a period of culture of 5 days in basal conditions, that is, without imposing BM-MSC developmental decisions by means of external growth factor supplementation. Firstly, we observe an explicitly dBone-associated upregulation of stem cell-related markers when compared with BM-MSC in control conditions and dECM models.

CXCL12 is a soluble ligand secreted by niche-resident BM-MSC reported to be highly involved in hematopoietic stem cells (HSC) communication and associated with cell-homing, especially during fracture healing.[94] To confirm the significancy of CXCL12 gene expression upregulation in the dBone condition, we further performed an immunostaining targeting protein expression of CXCL12 in BM-MSC seeded on the different substrates (Figure 6(a)). Interestingly, no expression of CXCL12 was detected in control or any dECM model. Contrarily, a high percentage of cells, but not all, cultured in the dBone model exhibited intracellular CXCL12 expression, corroborating the previous results toward a dBone-conferred niche-like environment for BM-MSC. Nestin is a recognized stem marker found in vivo particularly on BM-MSC at perivascular sites adjacent to the bone and marrow parenchyma, known to be closely associated with HSC communication in bone marrow.[95] Despite the high donor variance, the emerging transcription of Nestin, together with an increased gene expression of transcription factor Oct4 (p-value = 0.0651 to CS control), a factor well-known to be associated with pluripotency of stem cells,[96] as well as the enhanced CXCL12 expression at gene and protein level,[97] suggests that the 3D dBone model is capable to preserve the property of a primary BM stem cell niche, that is, to provide a sheltered environment for BM-MSC to maintain their stem phenotype. The supported stem-cell potential of recovered BM-MSC from decellularized bone models was functionally validated by a colony-forming unit (CFU) efficiency assay (Supplemental Figure S5a), where a slightly increased number of competent colony-forming cells was observed in dBone-recovered cells compared with controls. Moreover, a decreased level of Survivin mRNA in 3D dBone when compared to 2D cultures might be indicative of the structure-induced sheltered effect by protecting BM-MSC from external proliferation and mobilization stimuli, therefore allowing for the preservation of a rather quiescent phenotype.[98] In fact, cellular quiescence is a native key property of adult stem cells observed in vivo allowing BM-MSC to temporarily suppress proliferation but re-enter cell cycle upon stimuli.[99] However, literature regarding biology of quiescent BM-MSC in culture is poor due to the difficulty of maintaining the BM-MSC naïve phenotype during cell expansion in traditional culture-plastic surfaces.[26]

Next, we were interested to explore early microenvironment-related BM-MSC lineage commitment decisions. Thus, a selection of osteogenesis (Runx2, ALP and Col1) specific gene markers were investigated for BM-MSC at 5 day-basal culture on the different decellularized-models — whereas extensive long-term analysis of these markers should be further assessed in order to conclude about recognized differentiation potential of these constructs. Expression of Runx2 did not show to be predictive of the dECM material-osteoconductive properties previously observed. In principle, the time-point of analysis and the no-differentiation culture condition, were not sufficient to induce spontaneous detectable differences of the osteogenesis transcription factor by BM-MSC. Furthermore, no obvious trend was identified for gene expression of ALP in BM-MSC seeded either on control coverslips or in decellularized models nor in dBone models in basal conditions. To note, the osteoconductive function of dBone scaffolds was confirmed by cultivation in osteogenic medium and detection of ALP activity at day 7 (Supplemental Figure S5b). Col1 expression appears to present some donor-to-donor variability, yet while the collagen-rich dECM models seem to generally inhibit new formation of Col1 fibers on seeded BM-MSC, the native properties of dBone might induce synthesis of newly formed bone-matrix by BM-MSC (our previous results[25]), contributing to the augmentation of a cell-fitting niche. Additionally, there is evidence of BM-MSC osteoblastic differentiation induced by Col1-mediated $\alpha 2\beta 1$ integrin interaction through Runx2 transcriptional cascade activation.[100,101] Finally, a significant upregulation of SPP1 was detected in BM-MSC seeded in dBone. SPP1 expression is known to be particularly sensitive to physical environment and mechanical stimuli, possibly due to its dual role in cell adhesion[102] and ECM-calcium sequestering competence.[103]

In fact, early SPP1 mRNA and protein expression in response to mechanical cues has been strongly associated with bone remodeling process via osteoclast and osteoblast interaction,[104] also observed in our previous study on BM-MSC seeded in dBone.[25] Taken together, the results suggest that 2D dECM matrices are extremely accessible models which might be used as a BM-MSC culture substrate supporting their proliferation and differentiation potential. On the other hand, the 3D dBone model has shown to support the preservation of a naïve-like cell phenotype, hence providing a suitable in vitro model to study the overall functions of BM-MSC in a physiologically relevant microenvironment.

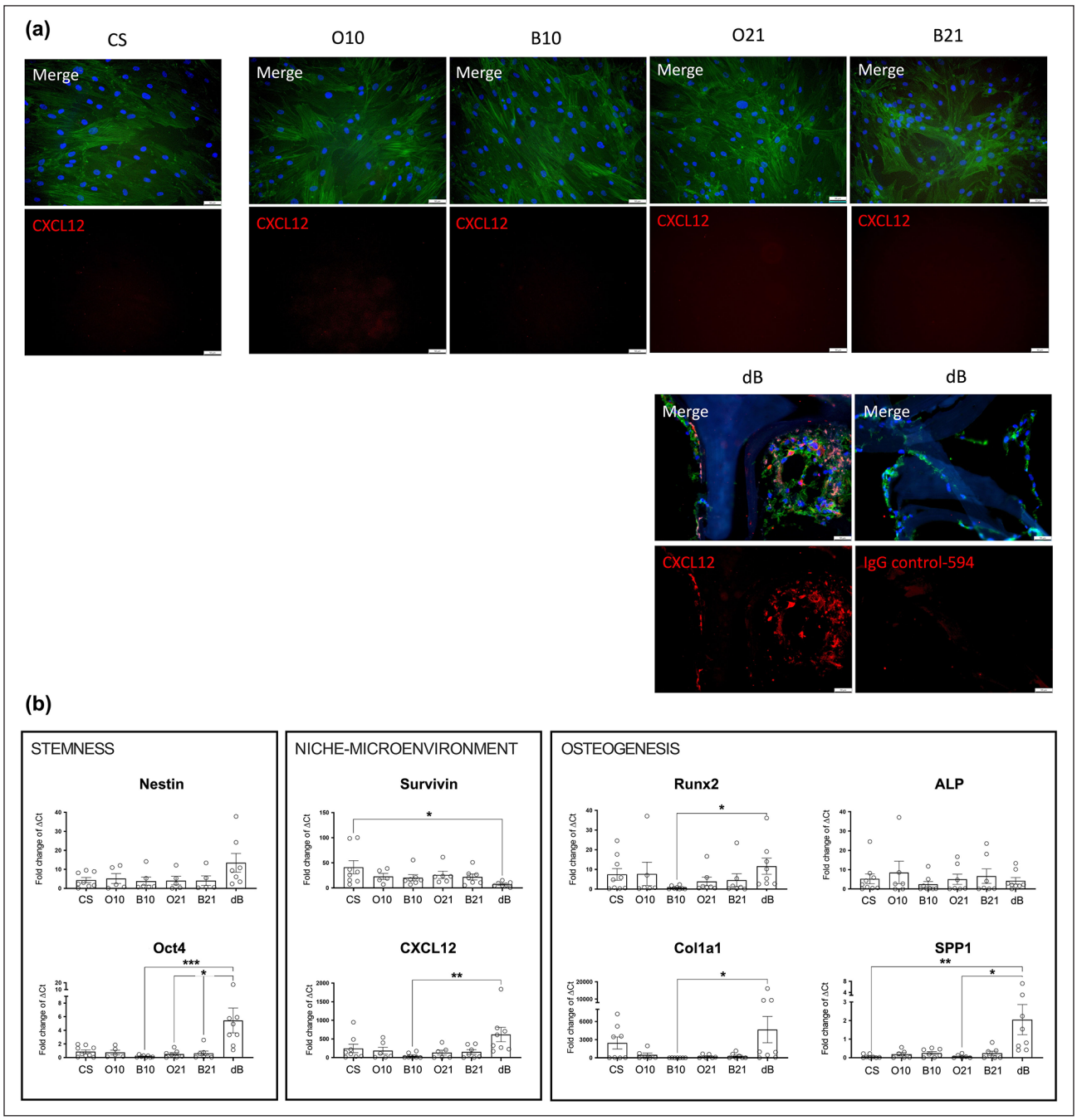

Figure 6. Analysis of the BM-niche signature of cells seeded in dECM and dBone models after 5 days in basal culture: (a) Representative images of CXCL12-stained samples ($n = 2$). Top panel: merge composite images of nuclei (DAPI, blue), F-actin (phalloidin, green) and CXCL12 (red) channels. Bottom panel: individual CXCL12-staining for better visualization. No observable signal in dECM models was detected, yet a strong intracellular staining in BM-MSC seeded in dBone was found. Absence of signal in secondary antibody control (on right) confirms the specificity of the secondary to the primary antibody and absence of sample auto-fluorescence. Scale bar: 50 µm. (b) Relative gene expression ($10^4 \times 2^{-}\Delta^{Ct}$) normalized to B2M housekeeping gene. A combination of genes associated with stemness: Nestin and Oct4; niche microenvironment cues: Survivin and CXCL12; and osteogenesis: Runx2, ALP, Col1 and SPP1 were analyzed. Statistics: Kruskal–Wallis one-way test, *$p < 0.05$, **$p < 0.01$, ***$p < 0.001$, $n = 4$–10.

Conclusion

The complexity of the extracellular matrix in adult stem cell niches and the relevance of its' different elements for MSC physiology remains elusive with the current in vitro manufactured alternatives, which cannot fully mimic the biochemistry and architecture of the native tissue-specific ECM. Decellularization of cell culture sheets and/or whole tissues may provide an alternative method to bypass these limitations. In this study, we showed that cell-derived

ECM models can be tailored by manipulating the cell culture conditions, particularly through biochemical additives during culture, in line with previous literature results. The established 2D dECM models proved to be a suitable culture substrate for BM-MSC, allowing cell-matrix interactions that more closely mimic the bone environment in vivo. The observed BM-MSC morphological shape changes suggested a superior cell adhesion to the substrates facilitated by the chemical properties of dECM models. Moreover, mature osteogenic day 21-matrices triggered spontaneous early osteogenic commitment of BM-MSC, where mineralization was detected in absence of external osteogenic differentiation factors. Furthermore, here we report on a 3D human-derived decellularized trabecular bone model developed in our laboratory as a promising scaffolding material to study the complexity of the bone skeletal environment. As far as we know, here we provided for the first time a comparative proteomic analysis between cell-derived dECM and human 3D dBone ECM, hence revealing key proteins involved in regulation of BM-MSC behavior and functions, such as adhesion, metabolic activity and osteogenic differentiation, raising new insights for the material functionalization of tissue engineering constructs. Interestingly, BM-MSC seeded in dBone scaffolds exhibited, when compared with control and dECM cultures, upregulation of BM stem cell-niche related genes, suggesting the recapitulation of the naïve BM-MSC phenotype.

Taken together, the here developed decellularization-based bone models, prominently the 3D dBone scaffold, seem to hold potential to provide a novel platform for advanced BM-MSC in vitro culture where mechanisms of activation, proliferation and lineage determination can be studied in a physiologically relevant context. Furthermore, future studies will focus on the investigation of the cellular interactions between MSC and their niche neighbor cells by means of co-culture systems using the here developed models.

Acknowledgements

We thank Dr. Andreas Schlosser (Rudolf-Virchow-Zentrum, Center for Integrative and Translational Bioimaging) for the help in the MS-proteomics data acquisition and analysis.

Author contributions

Conceptualization, M.H. and A.R.P.; investigation, A.R.P., P.S. and D.T.; resources, M.H., M.W., J.G..; original draft preparation, A.R.P..; review and editing, M.H., D.T. and P.S.; project administration, M.H.; funding acquisition, M.H. and J.G. All authors have read and agreed to the published version of the manuscript.

Declaration of conflicting interests

The author(s) declared no potential conflicts of interest with respect to the research, authorship, and/or publication of this article.

Funding

The author(s) disclosed receipt of the following financial support for the research, authorship, and/or publication of this article: This research was supported by the Interdisciplinary Center for Clinical Research (IZKF) at the University of Wuerzburg (Project D-361). We thank the Deutsche Forschungsgemeinschaft for funding the crossbeam scanning electron microscope Zeiss CB 340 (INST 105022/58-1 FUGG) within the DFG State Major Instrumentation Programme. This publication was supported by the Open Access Publication Fund of the University of Wuerzburg.

Ethical approval

The study was conducted according to the guidelines of the Declaration of Helsinki and approved by the Ethics Committee of the University of Wuerzburg (187/18). Informed consent was obtained from all subjects involved in the study.

ORCID iD

Marietta Herrmann https://orcid.org/0000-0002-2412-7474

Supplemental material

Supplemental material for this article is available online.

References

1. Friedenstein AJ, Deriglasova UF, Kulagina NN, et al. Precursors for fibroblasts in different populations of hematopoietic cells as detected by the in vitro colony assay method. *Exp Hematol* 1974; 2: 83–92.
2. Tuli R, Tuli S, Nandi S, et al. Characterization of multipotential mesenchymal progenitor cells derived from human trabecular bone. *Stem Cells* 2003; 21: 681–693.
3. Zuk PA, Zhu M, Ashjian P, et al. Human adipose tissue is a source of multipotent stem cells. *Mol Biol Cell* 2002; 13: 4279–4295.
4. Tondreau T, Meuleman N, Delforge A, et al. Mesenchymal stem cells derived from CD133-positive cells in mobilized peripheral blood and cord blood: proliferation, oct4 expression, and plasticity. *Stem Cells* 2005; 23: 1105–1112.
5. Sarugaser R, Lickorish D, Baksh D, et al. Human umbilical cord perivascular (HUCPV) cells: a source of mesenchymal progenitors. *Stem Cells* 2005; 23: 220–229.
6. Lee OK, Kuo TK, Chen W-M, et al. Isolation of multipotent mesenchymal stem cells from umbilical cord blood. *Blood* 2004; 103: 1669–1675.
7. In't Anker PS, Scherjon SA, Kleijburg-van der Keur C, et al. Isolation of mesenchymal stem cells of fetal or maternal origin from human placenta. *Stem Cells* 2004; 22: 1338–1345.
8. Murphy MB, Moncivais K and Caplan AI. Mesenchymal stem cells: environmentally responsive therapeutics for regenerative medicine. *Exp Mol Med* 2013; 45: e54–e54.
9. Gattazzo F, Urciuolo A and Bonaldo P. Extracellular matrix: a dynamic microenvironment for stem cell niche. *Biochimica et Biophysica Acta (BBA)-General Subjects* 2014; 1840: 2506–2519.
10. Bergfeld SA and DeClerck YA. Bone marrow-derived mesenchymal stem cells and the tumor microenvironment. *Cancer Metastasis Rev* 2010; 29(2): 249–261.

11. Herrmann M and Jakob F. Bone marrow niches for skeletal progenitor cells and their inhabitants in health and disease. *Curr Stem Cell Res Ther* 2019; 14: 305–319.
12. Jones DL and Wagers AJ. No place like home: anatomy and function of the stem cell niche. *Nat Rev Mol Cell Biol* 2008; 9(1): 11–21.
13. Schofield R. The relationship between the spleen colony-forming cell and the haemopoietic stem cell. *Blood Cells* 1978; 4: 7–25.
14. Brizzi MF, Tarone G and Defilippi P. Extracellular matrix, integrins, and growth factors as tailors of the stem cell niche. *Curr Opin Cell Biol* 2012; 24(5): 645–651.
15. Sacchetti B, Funari A, Remoli C, et al. No identical "mesenchymal stem cells" at different times and sites: human committed progenitors of distinct origin and differentiation potential are incorporated as adventitial cells in microvessels. *Stem Cell Reports* 2016; 6: 897–913.
16. Reilly GC and Engler AJ. Intrinsic extracellular matrix properties regulate stem cell differentiation. *J Biomech* 2010; 43: 55–62.
17. Hynes RO. The extracellular matrix: not just pretty fibrils. *Science* 2009; 326: 1216–1219.
18. Schultz GS and Wysocki A. Interactions between extracellular matrix and growth factors in wound healing. *Wound Repair Regen* 2009; 17: 153–162.
19. Midwood KS, Williams LV and Schwarzbauer JE. Tissue repair and the dynamics of the extracellular matrix. *Int J Biochem Cell Biol* 2004; 36: 1031–1037.
20. Lu P, Takai K, Weaver VM, et al. Extracellular matrix degradation and remodeling in development and disease. *Cold Spring Harb Perspect Biol* 2011; 3: a005058.
21. Guimarães CF, Gasperini L, Marques AP, et al. The stiffness of living tissues and its implications for tissue engineering. *Nat Rev Mater* 2020; 5: 351–370.
22. Dalby MJ. Topographically induced direct cell mechanotransduction. *Med Eng Phys* 2005; 27: 730–742.
23. Gjorevski N and Nelson CM. Bidirectional extracellular matrix signaling during tissue morphogenesis. *Cytokine Growth Factor Rev* 2009; 20: 459–465.
24. Loebel C, Mauck RL and Burdick JA. Local nascent protein deposition and remodelling guide mesenchymal stromal cell mechanosensing and fate in three-dimensional hydrogels. *Nat Mater* 2019; 18(8): 883–891.
25. Pereira AR, Lipphaus A, Ergin M, et al. Modeling of the human bone environment: mechanical stimuli guide mesenchymal stem cell-extracellular matrix interactions. *Materials* 2021; 14: 4431.
26. Bara JJ, Richards RG, Alini M, et al. Concise review: bone marrow-derived mesenchymal stem cells change phenotype following in vitro culture: implications for basic research and the clinic. *Stem Cells* 2014; 32: 1713–1723.
27. Herrmann M and Bara JJ. Biological changes in human mesenchymal stromal cells during monolayer culture. In: Atkinson K (ed.) *The biology and therapeutic application of mesenchymal cells*. Hoboken, NJ: John Wiley & Sons, 2016, pp.58–74.
28. Baker BM and Chen CS. Deconstructing the third dimension: how 3D culture microenvironments alter cellular cues. *J Cell Sci* 2012; 125: 3015–3024.
29. Lutolf MP and Hubbell JA. Synthetic biomaterials as instructive extracellular microenvironments for morphogenesis in tissue engineering. *Nat Biotechnol* 2005; 23: 47–55.
30. Pereira A, Trivanović D and Herrmann M. Approaches to mimic the complexity of the skeletal mesenchymal stem/stromal cell niche in vitro. *Eur Cell Mater* 2019; 37: 88–112.
31. Blache U, Stevens MM and Gentleman E. Harnessing the secreted extracellular matrix to engineer tissues. *Nat Biomed Eng* 2020; 4: 357–363.
32. Ramírez-Rodríguez GB, Pereira AR, Herrmann M, et al. Biomimetic mineralization promotes viability and differentiation of human mesenchymal stem cells in a perfusion bioreactor. *Int J Mol Sci* 2021; 22: 1447.
33. Hussey GS, Dziki JL and Badylak SF. Extracellular matrix-based materials for regenerative medicine. *Nat Rev Mater* 2018; 3: 159–173.
34. Stock UA and Schenke-Layland K. Performance of decellularized xenogeneic tissue in heart valve replacement. *Biomaterials* 2006; 27(1): 1–2.
35. Neumann A, Cebotari S, Tudorache I, et al. Heart valve engineering: decellularized allograft matrices in clinical practice. *Biomedizinische Technik/Biomedical Engineering* 2013; 58: 453–456.
36. Chen R-N, Ho HO, Tsai Y-T, et al. Process development of an acellular dermal matrix (ADM) for biomedical applications. *Biomaterials* 2004; 25: 2679–2686.
37. Brouki Milan P, Pazouki A, Joghataei MT, et al. Decellularization and preservation of human skin: a platform for tissue engineering and reconstructive surgery. *Methods* 2020; 171: 62–67.
38. Merguerian PA, Reddy PP, Barrieras DJ, et al. Acellular bladder matrix allografts in the regeneration of functional bladders: evaluation of large-segment ($>$ 24 cm2) substitution in a porcine model. *BJU Int* 2001; 85: 894–898.
39. Rosario DJ, Reilly GC, Ali Salah E, et al. Decellularization and sterilization of porcine urinary bladder matrix for tissue engineering in the lower urinary tract. *Regen Med* 2008; 3(2): 145–156.
40. Hoshiba T, Lu H, Kawazoe N, et al. Decellularized matrices for tissue engineering. *Expert Opin Biol Ther* 2010; 10: 1717–1728.
41. Smith CA, Board TN, Rooney P, et al. Correction: human decellularized bone scaffolds from aged donors show improved osteoinductive capacity compared to young donor bone. *PLoS One* 2017; 12: e0187783.
42. Duarte MM, Ribeiro N, Silva IV, et al. Fast decellularization process using supercritical carbon dioxide for trabecular bone. *J Supercrit Fluids* 2021; 172: 105194.
43. Taylor B, Indano S, Yankannah Y, et al. Decellularized cortical bone scaffold promotes organized neovascularization in vivo. *Tissue Eng Part A* 2019; 25: 964–977.
44. Duval K, Grover H, Han L-H, et al. Modeling physiological events in 2D vs. 3D cell culture. *Physiology* 2017; 32: 266–277.
45. Pereira AR, Rudert M and Herrmann M. Decellularized human bone as a 3D model to study skeletal progenitor cells in a natural environment. *Methods Cell Biol* 2020; 157: 123–141.

46. Cox J and Mann M. MaxQuant enables high peptide identification rates, individualized ppb-range mass accuracies and proteome-wide protein quantification. *Nat Biotechnol* 2008; 26: 1367–1372.
47. Carpenter AE, Jones TR, Lamprecht MR, et al. CellProfiler: image analysis software for identifying and quantifying cell phenotypes. *Genome Biol* 2006; 7: R100–R111.
48. Prewitz MC, Seib FP, von Bonin M, et al. Tightly anchored tissue-mimetic matrices as instructive stem cell microenvironments. *Nat Methods* 2013; 10: 788–794.
49. Marinkovic M, Block TJ, Rakian R, et al. One size does not fit all: developing a cell-specific niche for in vitro study of cell behavior. *Matrix Biol* 2016; 52-54: 426–441.
50. Cai R, Nakamoto T, Hoshiba T, et al. Matrices secreted during simultaneous osteogenesis and adipogenesis of mesenchymal stem cells affect stem cells differentiation. *Acta Biomater* 2016; 35: 185–193.
51. Zeitouni S, Krause U, Clough BH, et al. Human mesenchymal stem cell-derived matrices for enhanced osteoregeneration. *Sci Transl Med* 2012; 4: 132ra55–132ra155.
52. Chen XD, Dusevich V, Feng JQ, et al. Extracellular matrix made by bone marrow cells facilitates expansion of marrow-derived mesenchymal progenitor cells and prevents their differentiation into osteoblasts. *JBone Mineral Res* 2007; 22: 1943–1956.
53. Fernández-Pérez J and Ahearne M. Author correction: the impact of decellularization methods on extracellular matrix derived hydrogels. *Sci Rep* 2019; 9: 19818–19912.
54. Rossert J and de Crombrugghe B. Type I collagen: structure, synthesis, and regulation. In: Bilezikian J, Martin TJ and Rosen C (eds) *Principles of bone biology*. Leiden, The Netherlands: Elsevier, 2002, pp.189–XVIII.
55. Rico-Llanos GA, Borrego-González S, Moncayo-Donoso M, et al. Collagen type I biomaterials as scaffolds for bone tissue engineering. *Polymers* 2021; 13: 599.
56. Choi K-M, Seo Y-K, Yoon H-H, et al. Effect of ascorbic acid on bone marrow-derived mesenchymal stem cell proliferation and differentiation. *J Biosci Bioeng* 2008; 105(6): 586–594.
57. Robey PG and Boskey AL. The composition of bone. In: Rosen CJ (ed.) *Primer on the metabolic bone diseases and disorders of mineral metabolism*. 7th ed. Washington, DC: American Society for Bone and Mineral Research, 2008, 32–38.
58. Lin H, Yang G, Tan J, et al. Influence of decellularized matrix derived from human mesenchymal stem cells on their proliferation, migration and multi-lineage differentiation potential. *Biomaterials* 2012; 33: 4480–4489.
59. Guilak F, Cohen DM, Estes BT, et al. Control of stem cell fate by physical interactions with the extracellular matrix. *Cell Stem Cell* 2009; 5: 17–26.
60. Rozario T and DeSimone DW. The extracellular matrix in development and morphogenesis: a dynamic view. *Dev Biol* 2010; 341: 126–140.
61. Jiang X, Bruzewicz DA, Wong AP, et al. Directing cell migration with asymmetric micropatterns. *Proc Natl Acad Sci USA* 2005; 102: 975–978.
62. Doyle AD, Wang FW, Matsumoto K, et al. One-dimensional topography underlies three-dimensional fibrillar cell migration. *J Cell Biol* 2009; 184: 481–490.
63. McBeath R, Pirone DM, Nelson CM, et al. Cell shape, cytoskeletal tension, and RhoA regulate stem cell lineage commitment. *Dev Cell* 2004; 6: 483–495.
64. Treiser MD, Yang EH, Gordonov S, et al. Cytoskeleton-based forecasting of stem cell lineage fates. *Proc Natl Acad Sci USA* 2010; 107: 610–615.
65. Chen D, Sarkar S, Candia J, et al. Machine learning based methodology to identify cell shape phenotypes associated with microenvironmental cues. *Biomaterials* 2016; 104: 104–118.
66. Anlaş AA and Nelson CM. Tissue mechanics regulates form, function, and dysfunction. *Curr Opin Cell Biol* 2018; 54: 98–105.
67. Clark AG and Vignjevic DM. Modes of cancer cell invasion and the role of the microenvironment. *Curr Opin Cell Biol* 2015; 36: 13–22.
68. Marklein RA, Lo Surdo JL, Bellayr IH, et al. High content imaging of early morphological signatures predicts long term mineralization capacity of human mesenchymal stem cells upon osteogenic induction. *Stem Cells* 2016; 34: 935–947.
69. Prasad A and Alizadeh E. Cell form and function: interpreting and controlling the shape of adherent cells. *Trends Biotechnol* 2019; 37: 347–357.
70. Jaiswal N, Haynesworth SE, Caplan AI, et al. Osteogenic differentiation of purified, culture-expanded human mesenchymal stem cells in vitro.. *J Cell Biochem* 1997; 64: 295–312.
71. Dupont S, Morsut L, Aragona M, et al. Role of YAP/TAZ in mechanotransduction. *Nature* 2011; 474: 179–183.
72. Stein GS and Lian JB. Molecular mechanisms mediating proliferation/differentiation interrelationships during progressive development of the osteoblast phenotype. *Endocr Rev* 1993; 14: 424–442.
73. Ingber DE. Mechanical control of tissue growth: function follows form. *Proc Natl Acad Sci USA* 2005; 102: 11571–11572.
74. Dalby MJ, Gadegaard N and Oreffo RO. Harnessing nanotopography and integrin-matrix interactions to influence stem cell fate. *Nat Mater* 2014; 13: 558–569.
75. Murphy WL, McDevitt TC and Engler AJ. Materials as stem cell regulators. *Nat Mater* 2014; 13: 547–557.
76. Huang G, Li F, Zhao X, et al. Functional and biomimetic materials for engineering of the three-dimensional cell microenvironment. *Chem Rev* 2017; 117: 12764–12850.
77. Baroncelli M, van der Eerden BCJ, Chatterji S, et al. Human osteoblast-derived extracellular matrix with high homology to bone proteome is osteopromotive. *Tissue Eng Part A* 2018; 24: 1377–1389.
78. Alves RD, Demmers JA, Bezstarosti K, et al. Unraveling the human bone microenvironment beyond the classical extracellular matrix proteins: a human bone protein library. *J Proteome Res* 2011; 10: 4725–4733.
79. Viguet-Carrin S, Garnero P and Delmas PD. The role of collagen in bone strength. *Osteoporos Int* 2006; 17(3): 319–336.
80. Oono T, Specks U, Eckes B, et al. Expression of type VI collagen mRNA during wound healing. *J Investig Dermatol* 1993; 100: 329–334.

81. Sherman-Baust CA, Weeraratna AT, Rangel LB, et al. Remodeling of the extracellular matrix through overexpression of collagen VI contributes to cisplatin resistance in ovarian cancer cells. *Cancer Cell* 2003; 3: 377–386.
82. Theocharidis G, Drymoussi Z, Kao AP, et al. Type VI collagen regulates dermal matrix assembly and fibroblast motility. *J Investig Dermatol* 2016; 136: 74–83.
83. Ansorge HL, Meng X, Zhang G, et al. Type XIV collagen regulates fibrillogenesis: premature collagen fibril growth and tissue dysfunction in null mice. *J Biol Chem* 2009; 284: 8427–8438.
84. Niyibizi C, Visconti CS, Kavalkovich K, et al. Collagens in an adult bovine medial collateral ligament: immunofluorescence localization by confocal microscopy reveals that type XIV collagen predominates at the ligament-bone junction. *Matrix Biol* 1995; 14: 743–751.
85. Roberts AB, McCune BK and Sporn MB. TGF-beta: regulation of extracellular matrix. *Kidney Int* 1992; 41: 557–559.
86. Pan TC, Sasaki T, Zhang RZ, et al. Structure and expression of fibulin-2, a novel extracellular matrix protein with multiple EGF-like repeats and consensus motifs for calcium binding. *J Cell Biol* 1993; 123: 1269–1277.
87. Zhang Z, Zhang X, Zhao D, et al. TGF-β1 promotes the osteoinduction of human osteoblasts via the PI3K/AKT/mTOR/S6K1 signalling pathway. *Mol Med Rep* 2019; 19: 3505–3518.
88. Byron A, Humphries JD and Humphries MJ. Defining the extracellular matrix using proteomics. *Int J Exp Pathol* 2013; 94: 75–92.
89. Harvey A, Yen TY, Aizman I, et al. Proteomic analysis of the extracellular matrix produced by mesenchymal stromal cells: implications for cell therapy mechanism. *PLoS One* 2013; 8: e79283.
90. Brylka L and Jahnen-Dechent W. The role of Fetuin-A in physiological and pathological mineralization. *Calcif Tissue Int* 2013; 93: 355–364.
91. Herrmann M, Kinkeldey A and Jahnen-Dechent W. Fetuin-A function in systemic mineral metabolism. *Trends Cardiovasc Med* 2012; 22: 197–201.
92. Jahnen-Dechent W, Heiss A, Schäfer C, et al. Fetuin-A regulation of calcified matrix metabolism. *Circ Res* 2011; 108: 1494–1509.
93. Behnam K, Phillips ML, Silva JD, et al. BMP binding peptide: a BMP-2 enhancing factor deduced from the sequence of native bovine bone morphogenetic protein/non-collagenous protein. *J Orthop Res* 2005; 23: 175–180.
94. Sugiyama T, Kohara H, Noda M, et al. Maintenance of the hematopoietic stem cell pool by CXCL12-CXCR4 chemokine signaling in bone marrow stromal cell niches. *Immunity* 2006; 25: 977–988.
95. Xie L, Zeng X, Hu J, et al. Characterization of nestin, a selective marker for bone marrow derived mesenchymal stem cells. *Stem Cells Int* 2015; 2015: 762098.
96. Pan GJ, Chang ZY, Schöler HR, et al. Stem cell pluripotency and transcription factor oct4. *Cell Res* 2002; 12: 321–329.
97. Asada N, Kunisaki Y, Pierce H, et al. Differential cytokine contributions of perivascular haematopoietic stem cell niches. *Nat Cell Biol* 2017; 19: 214–223.
98. Singh P, Fukuda S, Liu L, et al. Survivin is required for mouse and human bone marrow mesenchymal stromal cell function. *Stem Cells* 2018; 36: 123–129.
99. Rumman M, Dhawan J and Kassem M. Concise review: quiescence in adult stem cells: biological significance and relevance to tissue regeneration. *Stem Cells* 2015; 33: 2903–2912.
100. Mizuno M, Fujisawa R and Kuboki Y. Type I collagen-induced osteoblastic differentiation of bone-marrow cells mediated by collagen-alpha2beta1 integrin interaction. *J Cell Physiol* 2000; 184: 207–213.
101. Elango J, Robinson J, Zhang J, et al. Collagen peptide upregulates osteoblastogenesis from bone marrow mesenchymal stem cells through MAPK- Runx2. *Cells* 2019; 8: 446.
102. Chen Q, Shou P, Zhang L, et al. An Osteopontin-Integrin interaction plays a critical role in directing adipogenesis and osteogenesis by mesenchymal stem cells. *Stem Cells* 2014; 32: 327–337.
103. Zappone B, Thurner PJ, Adams J, et al. Effect of Ca2+ ions on the adhesion and mechanical properties of adsorbed layers of human osteopontin. *Biophys J* 2008; 95: 2939–2950.
104. Morinobu M, Ishijima M, Rittling SR, et al. Osteopontin expression in osteoblasts and osteocytes during bone formation under mechanical stress in the calvarial suture in vivo. *J Bone Miner Res* 2003; 18: 1706–1715.